MASARYKOVA UNIVERZITA
Přírodovědecká fakulta
Ústav teoretické fyziky a astrofyziky

BAKALÁŘSKÁ PRÁCE

Aktivní galaxie měnící vzhled v rentgenovém oboru

Nikola Husáriková

Vedoucí bakalářské práce: RNDr. Jiří Svoboda, PhD

2021

Bibliografický záznam

Autor:	Nikola Husáriková Přírodovědecká fakulta, Masarykova univerzita Ústav teoretické fyziky a astrofyziky
Název práce:	Aktivní galaxie měnící vzhled v rentgenovom oboru
Studijní program:	Fyzika
Studijní obor:	Astrofyzika
Vedoucí práce:	RNDr. Jiří Svoboda, PhD
Akademický rok:	2020/21
Počet stran:	40
Klíčová slova:	Changing-look AGN, NGC 1566, X-ray variability

Bibliographic entry

Author:	Nikola Husarikova Faculty of Science, Masaryk University Department of Theoretical Physics and Astrophysics
Title of thesis:	Changing-look active galaxies in X-ray domain
Degree Programme:	Physics
Field of Study:	Astrophysics
Supervisor:	RNDr. Jiří Svoboda, PhD
Academic Year:	2020/21
Number of Pages:	40
Keywords:	Changing-look AGN, NGC 1566, X-ray variability

Moje poďakovanie patrí najmä mojej rodine, ktorá ma podporovala počas celého štúdia. Ďalej by som sa rada poďakovala Vaškovi Glosovi a Petrovi Gilarovi za povzbudenie pri písaní práce a užitočné gramatické a štylistické rady. Filipovi Hrochovi by som rada poďakovala za pomoc s prácou v *Python*-e a za podporu a motiváciu na každotýždenných bakalárskych dýchankoch vedených spolu s Romčou Grossovou. Norbertovi Wernerovi za rady a konzultácie a taktiež za prijatie do HEA skupiny a pravidelné meetingy. A nakoniec hlavne ďakujem vedúcemu práce Jiřímu Svobodovi za uvedenie do veľmi peknej a zaujímavej témy, za pravidelné konzultácie, za odpovede na všetky moje dotazy, za pomoc s angličtinou a za trpezlivosť počas celej doby ale najmä počas záverečných dní pred odovzdnaním.

Prohlašuji, že jsem svoji bakalářskou práci vypracovala samostatně pod vedením vedoucího práce a výhradně s použitím citovaných pramenů. Souhlasím se zapůjčováním práce a jejím zveřejňováním.

V Brně dne: Nikola Husáriková

. . . .

Abstrakt:

Aktivní galaxie měnící svůj vzhled, tzv. changing-look AGN, patří k velmi zajímavým objektům, kdy se náhle mění přítomnost širokých čar v optickém oboru, anebo dochází ke změnám rentgenového toku záření o několik řádů, nebo obojí. V této práci jsme analyzovali rentgenová pozorováni aktivní galaxie NGC 1566 s pomocí rentgenových observatoří XMM-Newton a NuSTAR. Potvrdili jsme prudké změny v toku záření o faktor 25 a zjistili nové, prudké změny v nedávných pozorováních. Prodiskutovali jsme několik možných interpretací tohoto chování.

Klíčová slova: Changing-look AGN, NGC 1566, X-ray variability

Abstract:

Changing-look active galaxies belong to very interesting objects because they are suddenly changing the presence of broad emission lines in the optical domain, or their X-ray flux is changing by several orders of magnitude, or both. In this thesis we analyse X-ray data of the active galaxy NGC 1566 with the observations taken by X-ray observatories XMM-Newton and NuSTAR. We confirm rapid X-ray flux changes by a factor of 25, and we found out another rapid changes in recent observations. We discuss few possible interpretations of this behaviour.

Keywords: Changing-look AGN, NGC 1566, X-ray variability

MUNI
SCI

MASARYKOVA UNIVERZITA
PŘÍRODOVĚDECKÁ FAKULTA
KOTLÁŘSKÁ 2, 611 37 BRNO
IČ: 00216224
DIČ: CZ00216224

ZADÁNÍ BAKALÁŘSKÉ PRÁCE

Akademický rok: 2020/2021

Ústav:	Přírodovědecká fakulta
Studentka:	Nikola Husáriková
Program:	Fyzika
Obor:	Astrofyzika

Ředitel *ústavu* PřF MU Vám ve smyslu Studijního a zkušebního řádu MU určuje bakalářskou práci s názvem:

Název práce:	Aktivní galaxie měnící vzhled v rentgenovém oboru
Název práce anglicky:	Changing-look active galaxies in X-ray domain
Jazyk závěrečné práce:	angličtina

Oficiální zadání:
Aktivní galaxie měnící svůj vzhled, tzv. changing-look AGN, patří k velmi zajímavým objektům, kdy se náhle mění buď jejich klasifikace v optickém oboru (z typu I an II či obráceně), nebo dochází ke změnám rentgenového toku záření o několik řádů, anebo obojí. Pokud by se jednalo o změny v akrečním stavu, pak jsou tyto změny relativně rychlé. Akreční stavy rentgenových dvojhvězd se mění v řádu několika měsíců. Superhmotné černé díry v centrech galaxií jsou více než milionkrát větší, a proto i časová proměnlivost by měla být milionkrát pomalejší. Přesto u těchto galaxií dochází k rapidním změnám v řádu několika měsíců až let. Předmětem této bakalářské práce bude shrnutí současného poznání okolo těchto proměnlivých galaxií, možná fyzikální interpretace jejich chování a rentgenová analýza vybraného zdroje, kterým je galaxie NGC 1566 s nedávnými pozorováními pomocí rentgenové observatoře Evropské kosmické agentury XMM-Newton.

Vedoucí práce:	RNDr. Jiří Svoboda, Ph.D.
Konzultant:	doc. Mgr. Norbert Werner, Ph.D.
Datum zadání práce:	23. 11. 2020
V Brně dne:	13. 6. 2021

Zadání bylo schváleno prostřednictvím IS MU.

Nikola Husáriková, 21. 1. 2021
RNDr. Jiří Svoboda, Ph.D., 26. 1. 2021
prof. Mgr. Jiří Krtička, Ph.D., 16. 2. 2021

Contents

Introduction

Active Galactic Nuclei have been always known as strongly variable sources across all wavelengths. Their luminosity can vary by an order of magnitude from months to hours. However, some of the changes are more dramatic – the source classification can be temporarily changed from one group to another one. An optical variability is often accompanied by the X-ray variability and in some cases, the source can change classification from Compton thick to Compton thin (and vice versa). An extreme X-ray variability suggests that interesting physical processes are happening in the cores of some AGNs. Unfortunately the mechanisms are still unknown. The prominent place in the AGN variability have changing-look AGNs. This phenomenon was once considered quite rare but with more and more surveys, the number of changing-look events is growing. The aim of the thesis is an X-ray spectral analysis of a local AGN NGC 1566 with observations obtained by X-ray observatories XMM-Newton and NuSTAR, and an interpretation in the frame its changing-look behaviour.

This thesis starts by introduction of the AGN unified model together with variability mechanisms proposed to happen in changing-look AGNs (chapter 1). In the chapter 2, we present long-term multi-wavelength investigation of the changing-look AGN of NGC 1566. In the third chapter (3), we describe detailed data reduction of observations taken by X-ray observatories XMM-Newton and NuSTAR. The chapter 4 contains our results of spectral analysis, which are then discussed in the chapter 5. At the ending chapter 6, we summarise our finding and conclusions.

Chapter 1

Theory

1.1 Active galactic nuclei

Observations[1] indicate that most galaxies have a supermassive black hole (SMBH) at its centres, which is also a case of the Milky Way. The typical mass of a SMBH in the centre of a galaxy is $\sim 10^7 - 10^9 \mathrm{M}_\odot$ (solar mass). The black hole radius (gravitational radius R_g) is defined as an event horizon, a region of space from which nothing can escape. It was firstly derived by Karl Schwarzschild:

$$R_\mathrm{g} = \frac{2GM}{c^2}, \tag{1.1}$$

where G is the gravitational constant, M is the mass of the object and c is the speed of light. SMBHs accrete the nearby gas environment, the mass has a non zero momentum, and therefore, it is assumed to accrete in the form of an accretion disc. If the SMBH is accreting large amount of surrounding matter, it is classified as an active galactic nuclei (AGN). The accretion disc luminosity often overwhelms the combined light of all of the galaxy stars. One of the main differences between regular galaxies and AGNs is that regular ones are mostly luminous in UV while AGNs are observable over all wavelengths from radio to X-rays.

There are many radiation mechanisms. Variations of the continuum emission in galaxies give us the masses of central black holes and upper limits on the sizes of their emitting regions and it also can give us clues about physical processes operating in the black hole region. A non-thermal power-law type hard X-ray emission has origin in the inverse Compton scattering of the disc photons by relativistic electrons in a

[1] This chapter is mostly motivated by the book An Introduction to Modern Astrophysics Carroll and Ostlie (2007).

hot plasma – corona. The optical/UV emission is the thermal blackbody radiation originating from an optically thick, geometrically thin, accretion disc. The X-ray emission could be reflected by the torus, the broad-line region and the disc. This reflection gives features like Compton hump peaking around 30–40 keV, or the iron Kα emission line at 6.4 keV (Matt et al. (1991)).

The matter of an accretion disc has a Keplerian velocity – an element of continuum is orbiting faster in the central region than an one in the outer region. The viscous friction arises due to these different orbital velocities, so interactions in the accretion disc heat-ups the disc causing emitting of the higher energetic radiation.

Several types of AGNs together with their main characteristics, are listed in Table 1.1. A classification of AGN types depends on AGNs orientation toward us as is shown in Figure 1.1. The figure also shows AGN's structure where the supermassive black hole is in the centre of a galaxy surrounded by an accretion disc, a dusty torus and both broad and narrow-line regions.

Table 1.1: Main properties of AGN types (where E-elliptical, S-spiral host galaxy). Credit: Norbert Werner personal communication.

Class	Host galaxy	Radio emission	Emission lines	Luminosity [erg s^{-1}]
Blazar	E	Strong	Weak	10^{45}–10^{49}
Radio-loud quasar	E	Strong	Broad	10^{45}–10^{49}
Radio galaxy	E	Strong	Narrow	10^{43}–10^{45}
Radio-quiet quasar	S/E	Weak	Broad	10^{45}–10^{49}
Seyfert 1	S	Weak	Broad	10^{43}–10^{45}
Seyfert 2	S	Weak	Narrow	10^{43}–10^{45}

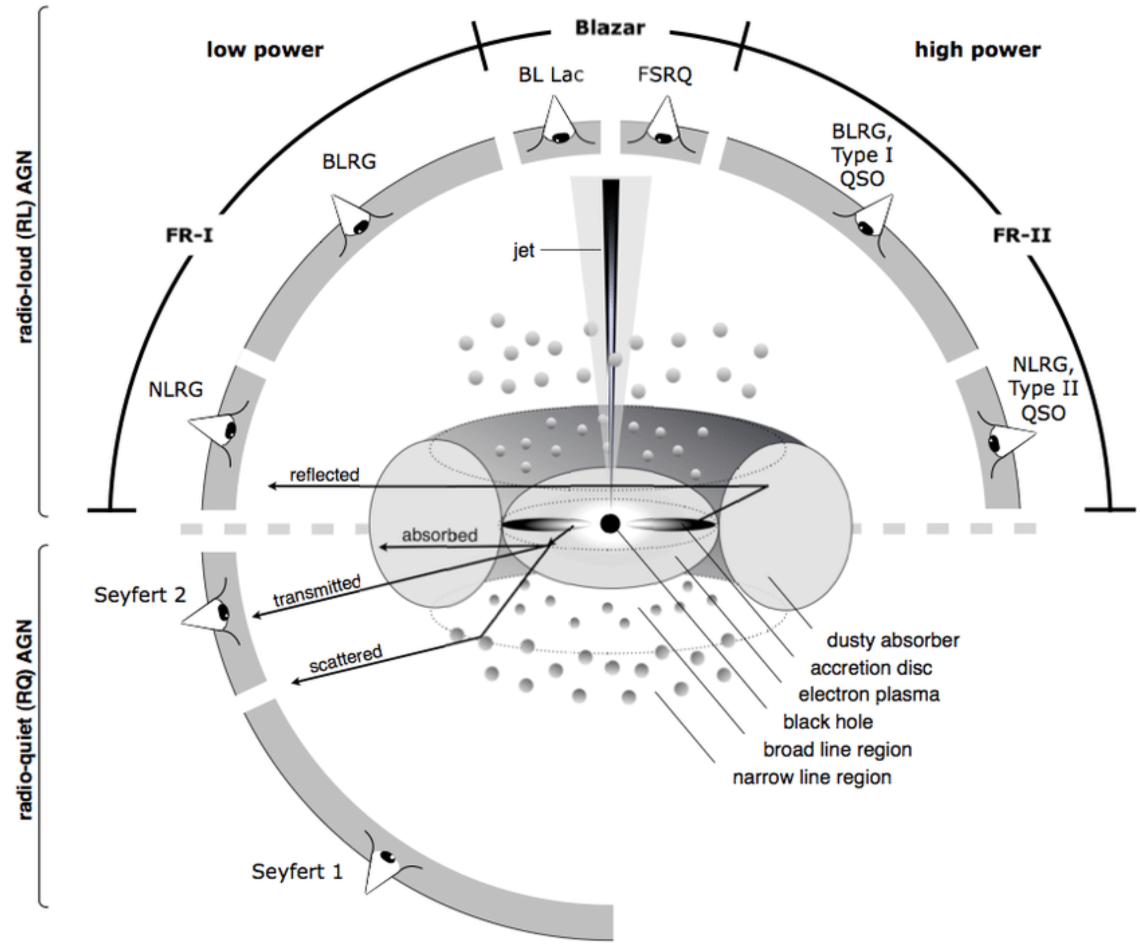

Figure 1.1: The Unified model of Active Galactic Nuclei. Credit: Beckmann and Shrader (2013).

1.2 Seyfert galaxies

Seyfert galaxies are named after their discoverer – astronomer Carl K. Seyfert who first started to study them in 1944. Both broad and narrow line regions are the main characteristic of Seyfert galaxies which we divide into two categories – Seyfert 1 (Sy1) and Seyfert 2 (Sy2).

This classification is based on the relative widths of broad components of Balmer lines as explained by the work of Khachikian and Weedman (1974). Nebular lines in the nuclei of Seyfert 1 galaxies are broad emission lines that include regular lines with a narrower forbidden core. Narrow lines are in both Sy1 and Sy2, but for Sy2 they are the only lines. Forbidden lines represent the low probability of transitions in atoms. Broad emission lines are broadened because they originate in the high-velocity region, while narrow lines originate from distant areas of the centre of the gravitational potential of the black hole. Osterbrock and Koski (1976) introduced also intermediate types like 1.2, 1.5 and so on.

The main confirmation of the unified model presented in Figure 1.1 in section 1.1 was made by Antonucci and Miller (1985) who discovered broad-line region in polarised light of Sy2 galaxy NGC 1068. It follows that the broad-line region in Sy2 is obscured by the optically thick surrounding medium called torus.

1.3 Changing-look AGNs

Changing-look AGNs (CL AGN) is a term for extremely variable AGNs (Matt et al. (2003)). These dramatic episodes can sometimes cause a temporary change of the source classification. As they summarized in Denney et al. (2014), the characterisation of CL AGNs was originally based on X-ray observations in which sources were changing from Compton-thick to Compton-thin or vice versa, over the years. If most of the X-ray photons are absorbed by surrounding torus of neutral hydrogen and dust with at least 1.5×10^{24} hydrogen atoms per cm^2, it is called Compton-thick AGN (Guainazzi (2002)). The classification was extended to optical spectrum changes when objects sometimes appear to have broad emission regions and sometimes not.

1.3.1 Observations

Optical variability

A recent example of a changing-look AGN in the optical domain was shown by Kollatschny et al. (2020), they present optical variability, as well as X-ray variability, of the Seyfert galaxy IRAS 23226-3843. Figure 1.2 shows its optical spectra. During the observing period from 1999 to 2017, it changed from a clear Seyfert 1 type to a Seyfert 1.9 type. Optical variability by a factor of 2 was accompanied by an X-ray continuum variability by a factor of 35. Extensive and successful search for CL AGNs was done by MacLeod et al. (2016), MacLeod et al. (2019). They found 27 optical variable changing look quasars and they present more than 200 candidates.

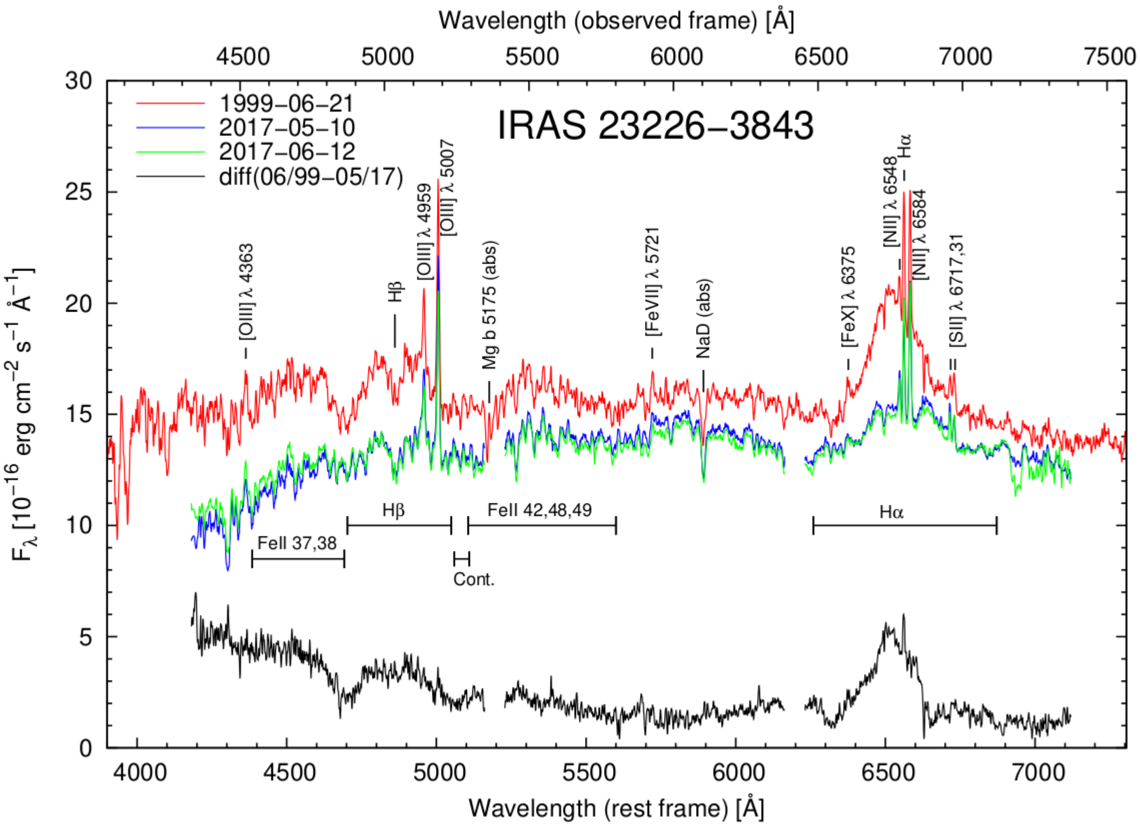

Figure 1.2: Optical spectra of IRAS 23226-3843 obtained in 2017 (green and blue) and 1999 (red) and also a difference between them (black). Credit: Kollatschny et al. (2020).

X-ray variability

Gaskell and Klimek (2003) explained that short timescale variability suggests of X-ray emission comes from a very small region close to the central black hole so-called corona. Middei et al. (2017) described that X-ray variability increases as a function of the time interval in which we investigate the sources.

In some cases this X-ray variability is extreme. For example, in the paper, Reeves et al. (2002) presented extreme X-ray variability in the quasar PDS 456 where X-ray flux doubled in only 30 ks. Another well-known object is Seyfert 1 galaxy IRAS 13224-3809 described in Boller et al. (1997) which increase brightness by a factor of 57 in just two days.

1.3.2 Physical interpretation of the observed variability

There are few theories about the origin of the variability, however, not all CL AGNs could be interpretable by a single mechanism. Rather a combination of them can be present.

Broad-line region occultation by obscuring material

An obscuring theory suggests that clumps of a cold gas from the torus can block AGN emission. As is shown in Figure 1.3, this theory can explain X-ray variability – X-ray emitting corona is compact ($\sim$ few black hole radii R_{g}) and so could be easily obscured by a thick cloud. However, it is not a satisfactory theory for the optical variability.

The optical emitting part of the accretion disc, and broad emission line region, are relatively large $> 1000\ R_{\mathrm{g}}$, therefore ones cannot be so easily obscured. Other features are in contradiction to this theory like differences in the behaviour of different emission lines.

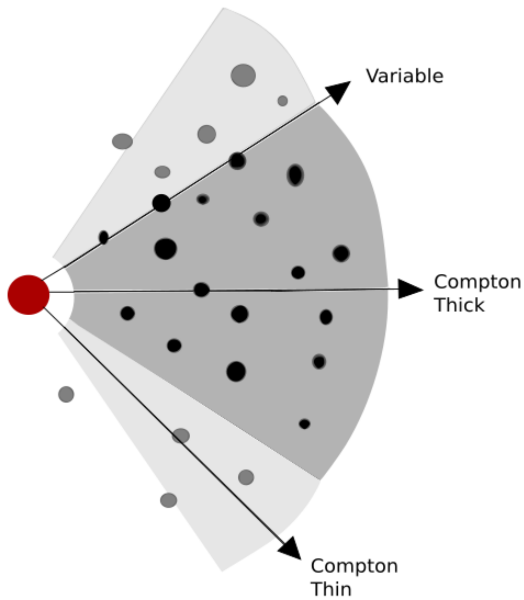

Figure 1.3: Model of obscuration by a Compton thin/thick medium. An X-ray variability is possible if emission comes through the border of these two media and clumps of an optically thick medium, which can move in the line of sight. Inspired by Risaliti et al. (2005) and Zhao figure [40].

Tidal disruption event

Tidal disruption events (TDEs) are one of the brightest transients in the optical, UV and X-rays sky Rossi et al. (2020). This occurs when the star comes into close vicinity of SMBH so it is tidally disrupted and consumed by the SMBH. These events can produce significant flares, peaking in much less than a year and a fading could be potentially observable for a few years Saxton et al. (2018). An emission of TDE's is in the UV or soft X-rays (0.1–2.4 keV).

Spectral state changes

Most AGN, show no variability, or just minimal, over long decades, suggesting that they remain in the same spectral state. Spectral state changes are discussed by Körding et al. (2006), Sobolewska et al. (2011) or Svoboda et al. (2017) who compared accreting SMBHs to XRB.

They both harbours accreting black holes, an accretion disc emitting thermal radiation, and a non-thermal X-ray emitting corona. XRBs evolve more rapidly and their evolution can be traced in the hardness-intensity diagram (Fender et al. (2004)). The diagram displays how they evolve from low-hard, through high-hard, high-soft back to the low-hard states. Different spectral states could possibly explain the AGN radio-dichotomy (Svoboda et al. (2017)). The radio-loud low-luminosity AGNs corresponds to the low-hard, and radio-loud quasars with high-luminosity to high-hard states of XRBs. Bright Seyfert galaxies correspond to soft states.

The transitions of state of the galactic black hole binaries occurs on time-scales of hours or shorter. It is thought that transitions time-scales corresponds of masses of black holes therefore, for the supermassive black holes, it should operate at time-scales $\sim 10^5$ years. Time scales of variability (where α is a disc viscosity parameter, H height and R radius of an accretion disc):

$$t_{\mathrm{dynamic}} = \alpha R^{\frac{3}{2}} M^{-\frac{1}{2}} \;\approx\; 10 \text{ days} \tag{1.2}$$

$$t_{\mathrm{thermal}} = t_{\mathrm{dynamic}}/\alpha \;\approx\; 3 \text{ months} \tag{1.3}$$

$$t_{\mathrm{viscous}} = t_{\mathrm{thermal}} \left(\frac{H}{R}\right)^{-2} \;\approx\; 1 \text{ Myr} \tag{1.4}$$

Observed variabilities are on time-scales of several years. Whereas some of the characteristics of AGNs and XRBs are not so similar; they have different disc properties like densities and ionisations, AGNs have the X-ray structure – corona, and AGNs are no isolated systems like XRBs. Because of these differences, AGN spectral change time scale approximations to those of XRBs could operate slightly different.

Accretion disc instabilities

We briefly summarise types of accretion disc instabilities with references; see Mineshige (1993), Habibi and Abbassi (2019) for more detailed information.

The partial ionisation process of hydrogen causes observable effects in stars, but it very likely produces visible effects in accretion discs as well. The mechanism which causes outbursts of dwarf novae, soft X-ray transients, or low mass X-ray binaries is called the thermal limit-cycle instability. If the radiation pressure dominates over gas, accretion discs are thermally and viscously unstable. An optically thin disc can have a proton temperature higher than the electron. In this case, the disc plasma can alternate between the two-temperature state, and the one-temperature state, thereby modulate hard X-ray intensities. The presence of wind, and magnetic field, in a thin accretion disc can also destabilises the disc. All of these instabilities can produce changes in the accretion flow and, often, dramatic variations of the accretion luminosity.

Chapter 2

NGC 1566

2.1 Characteristics

NGC 1566, nicknamed – The Spanish Dancer, is a local face-on spiral Seyfert galaxy with strong spiral arms (see Figure 2.1). With redshift z=0.005 (D=7.2 Mpc), it is the nearest changing-look AGN (Oknyanskij et al. (2018)). Its discoverer on May 28, 1826 was Scottish astronomer – James Dunlop. NGC 1566 is usually classified as Seyfert 1.5 galaxy, and is the second brightest Seyfert galaxy known. The study of NGC 1566 began in 1960 and its variability was discovered in 1969 by Pastoriza and Gerola (1970).

Figure 2.1: Hubble space telescope image of NGC 1566. Credit: NASA, ESA, Hubble, Leo Shatz (taken from – web [27]).

2.2 Multi-wavelength variability

Pastoriza and Gerola (1970) compared spectra of NGC 1566 from different epochs (see 2.2a). Hβ line was stronger in archival observation, while in 1969 the N_1 and N_2 (5007 Å and 4959 Å nebula lines of [OIII]) are clearly observable, and Hβ is very weak. The first optical light curve published by Quintana et al. (1975) confirms spectral variations; the optical luminosity of the nucleus varies by a full magnitude in time scales of one year as is shown in Figure 2.2b. The object became "weak Seyfert" for the next 12 years. Re-brightening of Hβ became observable in the period 1982–1991 but none of them was such strong as the outburst in 1962 (Oknyanskij et al. (2018)). Another strong outburst occurred in July 2018. The optical spectrum was dramatically changed (Ochmann et al. (2020)) as is shown in Figure 2.3a. This outburst was also observed as a dramatic increase in X-ray flux (Parker et al. (2019)). After a period of quiescence, the spectrum increased in brightness by a factor of 30–40 in a short time period, see Figure 2.3b. Oknyanskij et al. (2018) presented the long-term multi-wavelength variability with some significant re-brightening obtained in the post-maximum period 2018–2019. Figure 2.4 shows their Swift observations with three visible outbursts during 2019.

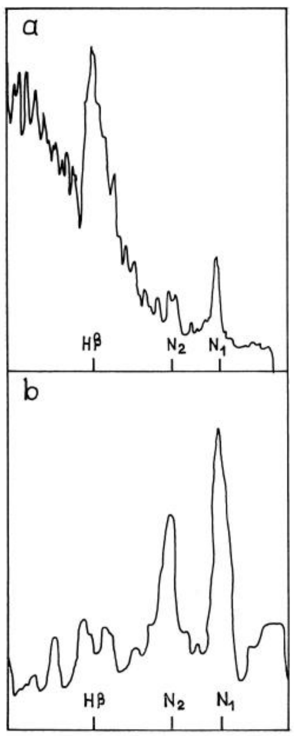

(a) Credit: Pastoriza and Gerola (1970).

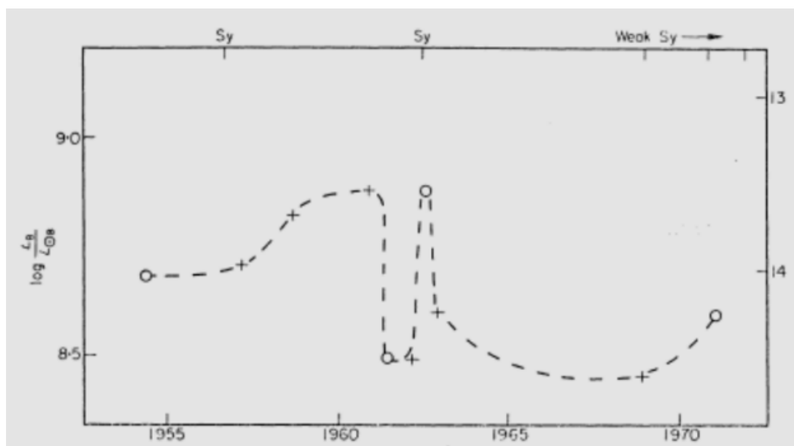

(b) Credit: Quintana et al. (1975).

Figure 2.2: Left: (a)-up An original spectrum obtained by Shobbrokk in 1962. (b)-bottom The spectrum obtained in 1969 by Pastoriza and Gerola. Right: B-magnitude variation of the nucleus of NGC 1566.

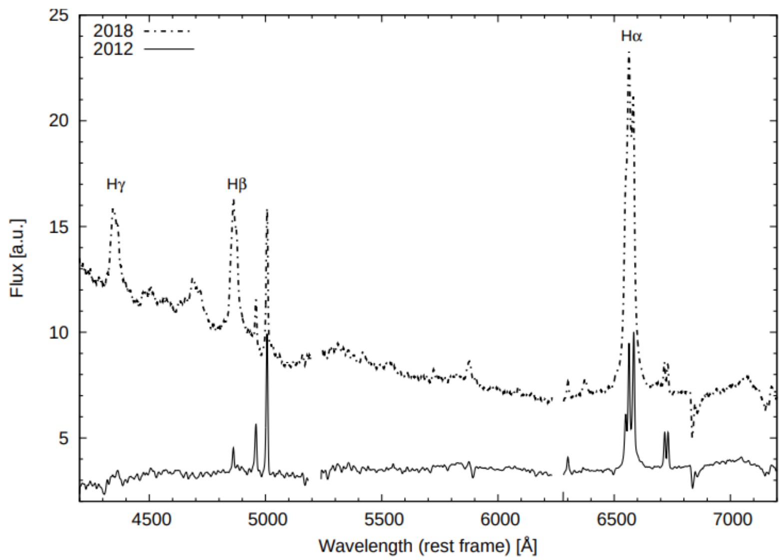

(a) Credit: Ochmann et al. (2020).

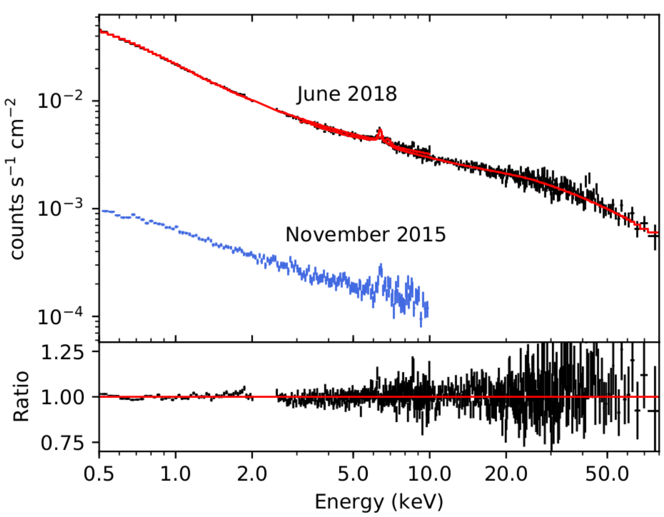

(b) Credit: Parker et al. (2019).

Figure 2.3: (a) Optical spectra of NGC 1566 in its low state (2012) and in its high state after the outburst (2018). Broad-band XMM-Newton and NuSTAR spectrum of NGC 1566.

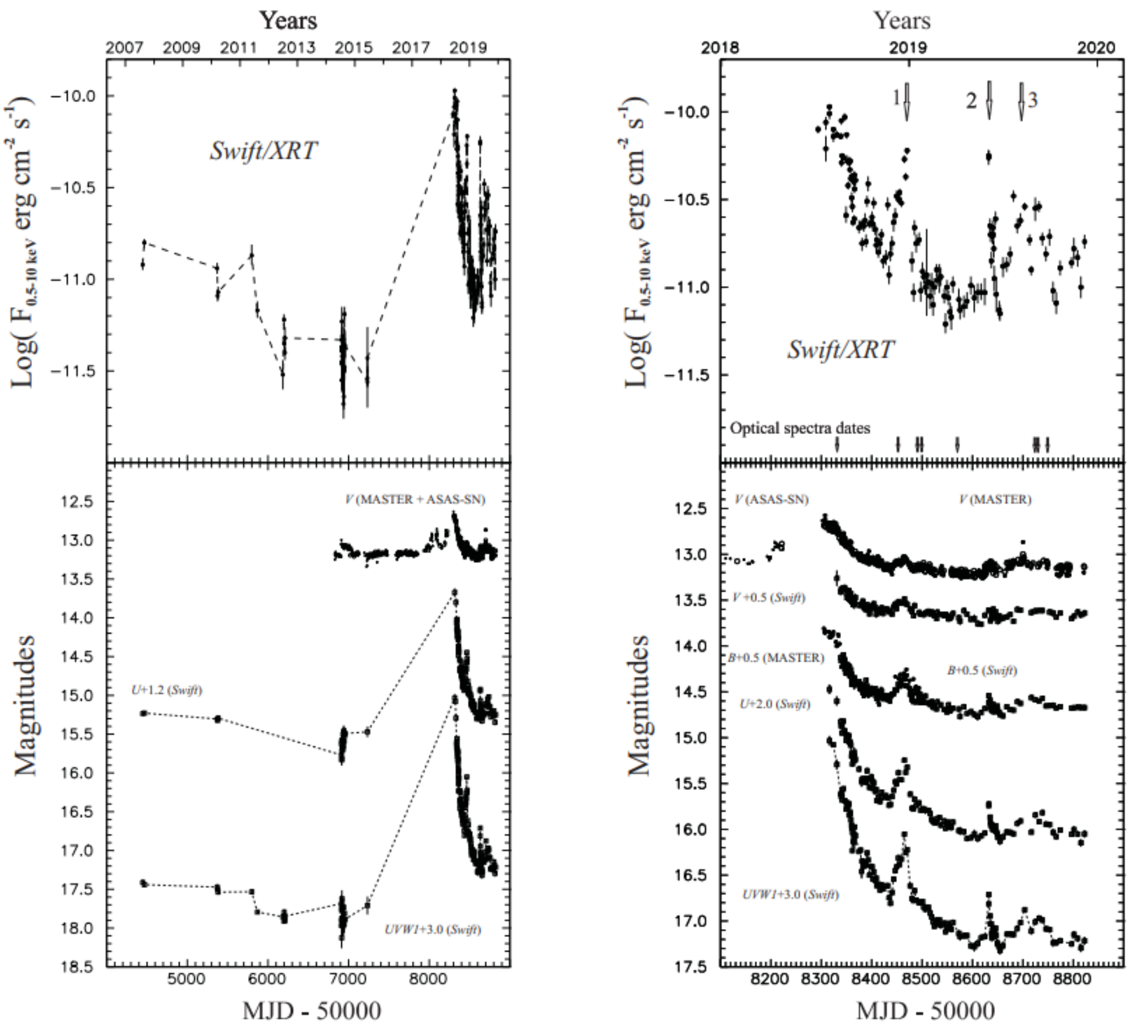

Figure 2.4: Top panels show Swift/XRT 0.5–10 keV X-ray flux, bottom panels show optical-UV observations. The left panel is a comparison with a previous time period, while the right panel is only post-maximum 2018–2019 period. Credit: Oknyanskij et al. (2018).

Chapter 3

Data reduction of NGC 1566

This section describes data reduction of X-ray observations of NGC 1566.

3.1 X-ray observatories

XMM-Newton

The European Space Agency's (ESA) X-ray Multi-Mirror Mission (XMM-Newton) was launched by Ariane 504 rocket launcher on December 10th 1999 (website [24]). The telescope was named to honour one of the most famous scientists, Sir Isaac Newton, the man who invented spectroscopy. It is still in the operation to this date, and prolonged to work through 2028. The satellite orbits Earth every 48 hours, so allowing long period observations. The 4 tonnes and 10 m long XMM-Newton is carrying three types of X-ray instrument. Its schema is shown in Figure 3.1. Two of the cameras are Metal Oxide Semi-conductors (MOS cameras) which consist of an array of 7 CCDs (600 $\times$ 600 pixels each). They are mounted behind X-ray telescopes equipped with Reflection Grating Spectrometers (RGS). The third X-ray telescope is an array of 12 pn CCDs (64 $\times$ 200 pixels each) so-called pn camera. Its design provides a large collecting area of $\sim$ 120 m^2 and offers very sensitive imaging observations. The energy range is from 0.5 to 12 keV with an angular resolution of 6 arcsec.

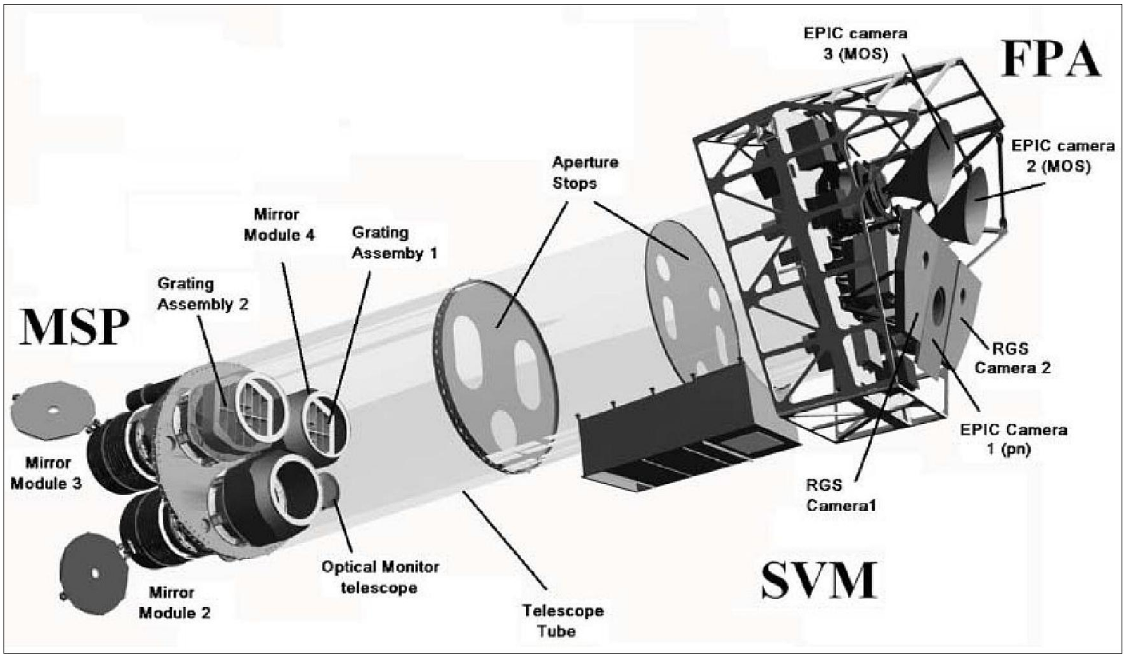

Figure 3.1: XMM-Newton scheme. Credit: ESA webpage [7]

NuSTAR

The Nuclear Spectroscopic Telescope Array (NuSTAR) mission, launched on a Pegasus rocket on June 13 2013, is the first focusing hard X-ray telescope in orbit. The two meters long telescope has two detectors units, each at the focus of one of the two co-aligned NuSTAR optics units. The focal plane bench consists of two solid state photon counting detector modules – FPMA and FPMB. NuSTAR operates in the band from 3 to 79 keV. It provides an angular resolution of 9.5 arcsec.

3.2 Observations and data reduction

We analyse X-ray observations of NGC 1566 performed in 2015–2019 by XMM-Newton and NuSTAR. Details of 5 XMM-Newton observations are listed in Table 3.1. Recent 4 observations were quasi-simultaneously observed also by NuSTAR (see Table 3.2). Data are processed with HEASoft version 6.28 and Science Analysis System (SAS) version 18.0.0.

Table 3.1: XMM-Newton observations

Observation ID	Start date	Duration [s]
0763500201	2015–11–05 01:49:16	91900
0800840201	2018–06–26 23:55:24	94200
0820530401	2018–10–04 12:34:16	108000
0840800401	2019–06–05 07:53:14	94000
0851980101	2019–08–11 16:27:46	17999

Table 3.2: NuSTAR observations

Observation ID	Start date	Duration [s]
80301601002	2018–06–26 20:06:09	56836
80401601002	2018–10–04 12:16:09	75395
80502606002	2019–06–05 07:46:09	57262
60501031002	2019–08–08 11:26:09	58922

3.2.1 XMM-Newton

Observation data files (ODF) were downloaded from the XMM-Newton archive [8]. These files include raw event science files due the EPIC cameras. We followed the step-by-step data reduction procedure that is described on the ESA website [9]. To initialise SAS we have to define three variables: *SAS_ CCPATH* (which is a path to calibration files), *SAS_ CCF* and *SAS_ ODF*. Then we made the calibration index file with the SAS task *cifbuild* and finally the summary file with *odfingest*. After these steps, we were ready to reprocess ODFs to the calibrated EPIC event list with *emproc* for EPIC-MOS and *epproc* for EPIC-pn. These event lists allow us to generate images and spectra with *evselect*.

The further procession is slightly different for each observation so we describe it separately and chronologically. Each observation, except the last one, contains data from three detectors – MOS1, MOS2 and pn. We describe the data reduction procedure on the first observation. For the other observations, we list only used values or some specific problems because the procedure is the same. Specific values for each observation like source and background regions, threshold and clean exposure time are listed in tables 3.3 and 3.4.

The ideal background region should be determined from a region larger than the source region. However, in our case, we mostly use smaller background regions because EPIC cameras were operating in a small window mode to avoid piled-up data of bright sources.

The "Full frame" mode means that all pixels of all CCDs are operating so the full field of view is covered. In a "Small Window" is reading out only a part of the MOS CCD chip and only a part of the one (CCD number 4) of 12 pn CCDs is used to collect data.

Images obtained for determination of the source (red circles) and background (green circles) regions for each observation are shown in Figures 3.5, 3.6, 3.7, 3.8 and 3.9. Physical coordinates of the centres of source, and background regions for XMM-Newton observations, are listed in Tables 3.5, 3.6.

We start with the first XMM-Newton observation taken on November 5 2015. We made the Good Time Interval (GTI) file which contains an EPIC filtered event list filtered for the high background flaring. In Figure 3.2, we can see the background light curve which we plot with *dsplot*, from which we choose a threshold just above the value where the light curve is low and steady, which will select only GTI. The reason why we are doing that is to avoid misidentification of hot pixels as high energy events. This process cuts the observation duration to a clean exposure time. Used threshold

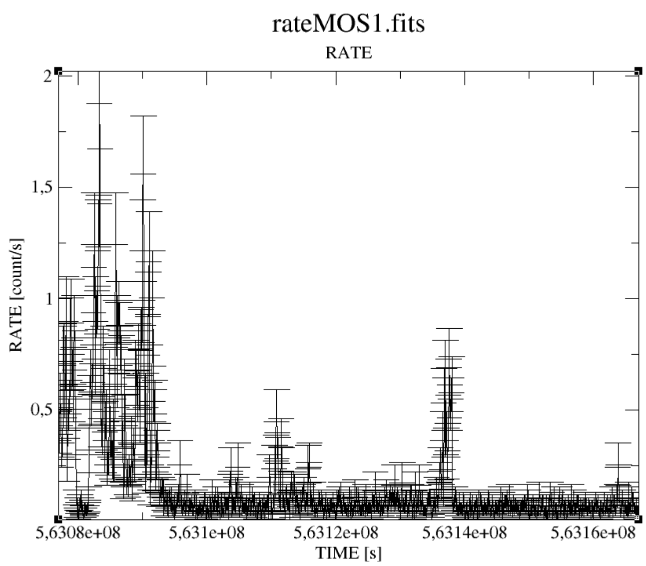

Figure 3.2: An example of the background light curve

is 0.35 counts s^{-1} for MOS1, 0.3 counts s^{-1} for MOS2 and 0.4 counts s^{-1} for pn. Clean exposure time is 78 ks for both MOS1 and MOS2 and 55 ks for pn. For these three detectors, we obtain images which are shown in Figure 3.5. We display them with the SAOImageDS9 astronomical imaging and data visualization application. We determine both source and background region from images. We extract source photons from a 30 arcsec radius circle around the nominal position of the source in all three EPIC detectors. The background region was selected by 40 arcsec radius circle for MOS1 and MOS2, and 70 arcsec for pn. We check if the data are no piled up with task *evselect*. The task *epatplot* allows us to plot a graph where we can search for pile-ups. The data seems to be un-affected. We extract source and background spectra with *evselect*. We generate a redistribution matrix with task *rmfgen* and an ancillary file with *arfgen*.

The data from observation taken on June 26 2018 were piled up so we take an annulus source region with the 30 arcsec outer and 8 arcsec inner radius for all three detectors. Comparison between piled-up and un-affected data is shown in Figure 3.3. The last of our analysed observations were taken on August 11 2019. For this observation, we have data only from MOS2 and the pn detector. The duration of the observation is originally very short, but after filtering of a flaring background, it is even shorter. Figure 3.4 shows that the background light curve is not very low and steady. The threshold is set to good represent values, 0.35 counts s^{-1} for MOS2 and 0.4 counts s^{-1} for pn. A clean exposure time is 5 ks for MOS2 and only 560 s for pn. The observation seems to be affected by high background flares. Finally, we rebin all of the spectra to signal to noise S/N ratio by a factor of 6 and to oversample the data by a factor of 3 with the SAS task *specgroup*.

Table 3.3: Selected threshold and final exposure time (Exp).

Date	MOS1 Threshold [counts s^{-1}]	MOS1 Exp [ks]	MOS2 Threshold [counts s^{-1}]	MOS2 Exp [ks]	pn Threshold [counts s^{-1}]	pn Exp [ks]
November 2015	0.35	78	0.3	78	0.4	55
June 2018	0.35	90	0.35	90	0.4	65
October 2018	0.35	103	0.35	103	0.4	74
June 2019	0.2	87	0.35	88	0.4	64
August 2019	–	–	0.35	5	0.4	1

Table 3.4: Radius of selected source and background regions in arcsec.

Date	MOS1		MOS2		pn	
	Source	Background	Source	Background	Source	Background
November 2015	30	40	30	40	30	70
June 2018	30; 8	11	30; 8	10	30; 8	40
October 2018	30	10	30	12	30	33
June 2019	30	10	30	9	30	40
August 2019	–	–	30	40	30	40

Table 3.5: Physical coordinates of centres of source regions for XMM-Newton observations.

Date	MOS1	MOS2	pn
November 2015	26844.633, 24138.653	26820.464, 24123.523	26840.200, 24125.554
June 2018	24079.695, 26631.732	24000.784, 26638.259	24050.858, 26690.864
October 2018	25753.96, 23871.966	25779.149, 23849.016	25764.311, 23811.197
June 2019	24121.554, 26765.721	24110.647, 26776.795	24128.928, 26769.185
August 2019	–	24308.414, 24640.031	24314.795, 24693.314

Table 3.6: Physical coordinates of centres of background regions for XMM-Newton observations.

Date	MOS1	MOS2	pn
November 2015	24812.919, 29809.592	23784.055, 29504.217	45306.716, 33324.303
June 2018	24889.716, 27997.344	25164.755, 26041.128	27116.302, 29584.105
October 2018	24381.835, 24201.942	24643.044, 24125.242	22237.029, 25607.140
June 2019	25112.441, 28033.533	23141.389, 27469.121	27113.551, 29288.672
August 2019	–	27377.012, 26179.717	29601.842, 28662.476

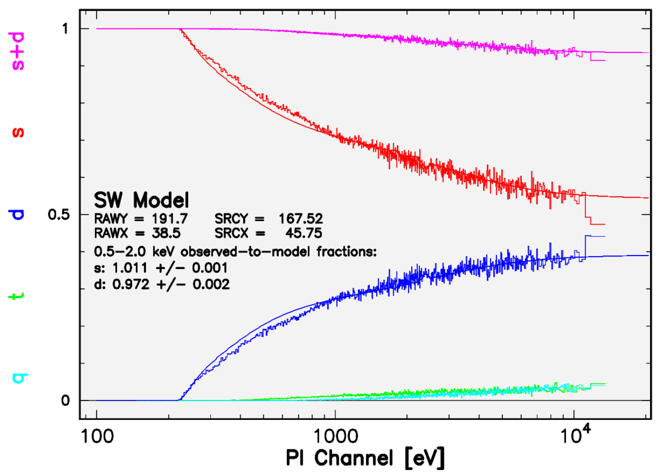

(a) Data affected by pile-up

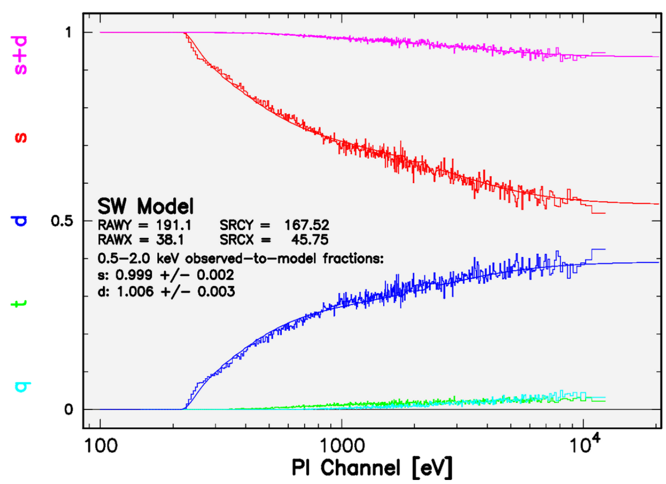

(b) Not affected data

Figure 3.3: Comparison between affected and un-affected data by a pile-up. Different coloured letters mean different types of events. S as singles, d – doubles, t – triples, q – quadruples, s+d as singles plus doubles.

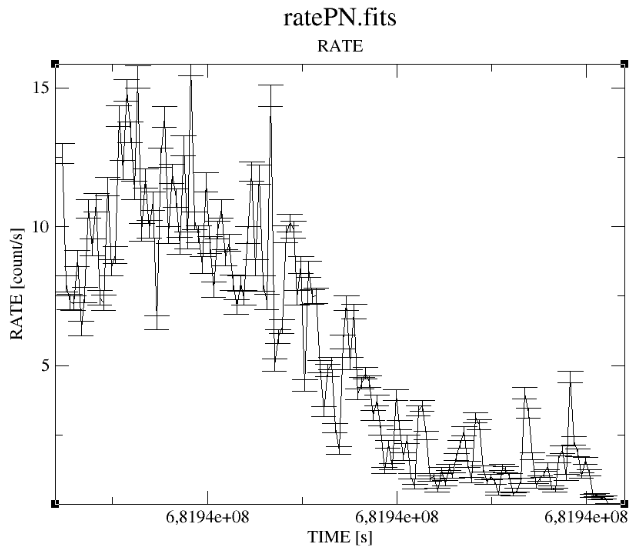

Figure 3.4: Background light curve obtained for observation taken on August 11 2019

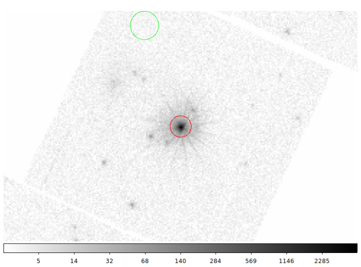

(a) MOS1

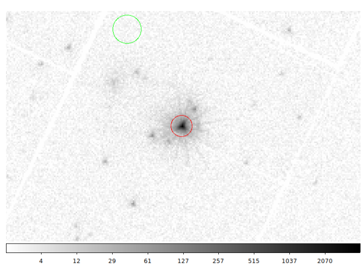

(b) MOS2

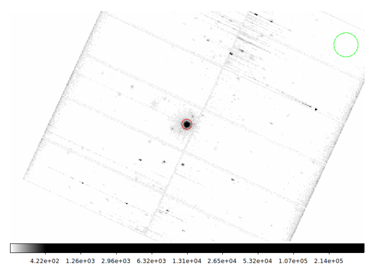

(c) pn

Figure 3.5: Images obtained from the observation taken on November 5 2015

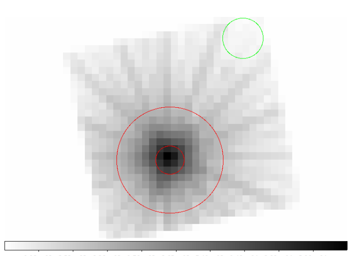

(a) MOS1

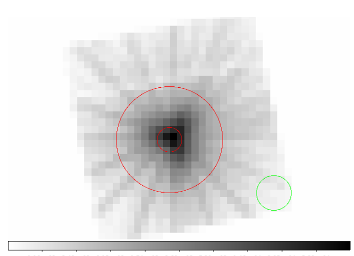

(b) MOS2

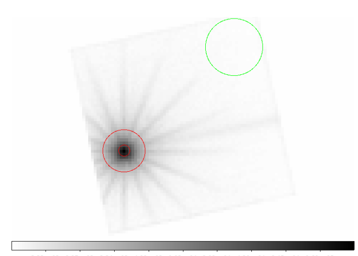

(c) pn

Figure 3.6: Images obtained from the observation taken on June 26 2018

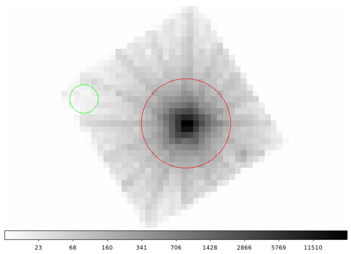

(a) MOS1

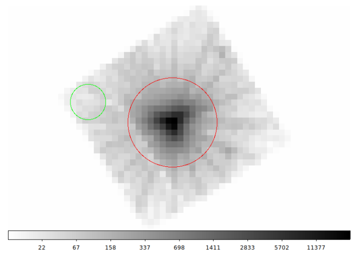

(b) MOS2

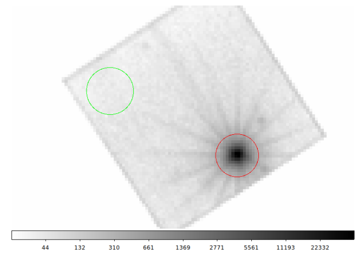

(c) PN

Figure 3.7: Images obtained from the observation taken on October 4 2018

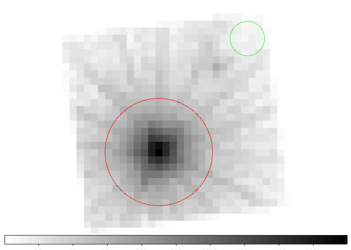

(a) MOS1

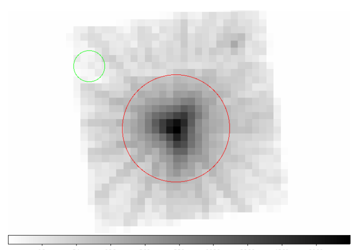

(b) MOS2

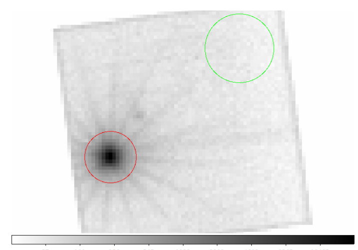

(c) PN

Figure 3.8: Images obtained from the observation taken on June 5 2019

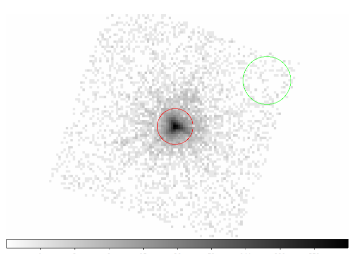

(a) MOS2

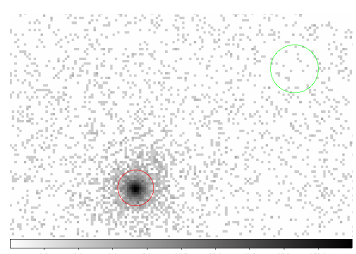

(b) PN

Figure 3.9: Images obtained from the observation taken on August 11 2019

3.2.2 NuSTAR

We download the NuSTAR data from the NuSTAR archive [26]. For the data processing, we use NuSTARDAS version 2.0.0. We process the data with the guide on NASA's HEASARC website [25]. With the task *nupipline*, we produce Level 2 event files which means that they are calibrated and cleaned using Good Time Intervals. Figures 3.10, 3.11, 3.12 and 3.13 show obtained images from which we determine 30 arcsec radius circle source and 90 arcsec radius circle background region for every observation from detectors FPMA and FPMB. Coordinates of centres of source and background regions for NuSTAR observations are listed in Tables 3.7 and 3.8. We extract source spectra with the task *nuproducts* and bin them to a signal to noise S/N ratio of 6 with *grppha*. A clean exposure time is the same as the original one.

Table 3.7: Coordinates of centres of source regions for NuSTAR observations.

Date	FPMA	FPMB
June 2018	4:20:00.4159, –54:56:17.113	4:20:00.8776, –54:56:11.434
October 2018	4:19:59.9205, –54:56:19.428	4:20:00.5186, –54:56:23.780
June 2019	4:20:00.4065, –54:56:16.357	4:20:00.5946, –54:56:11.650
August 2019	4:20:00.3839, –54:56:20.210	4:20:01.1004, –54:56:19.244

Table 3.8: Coordinates of centres of background regions for NuSTAR observations.

Date	FPMA	FPMB
June 2018	4:19:19.4331, –54:49:41.055	4:19:23.8799, –54:49:25.620
October 2018	4:21:00.7285, –54:50:34.438	4:20:57.6673, –54:50:55.510
June 2019	4:19:05.6121, –54:51:42.823	4:19:06.0292, –54:50:42.991
August 2019	4:19:58.6842, –54:47:24.341	4:20:02.2402, –54:47:33.210

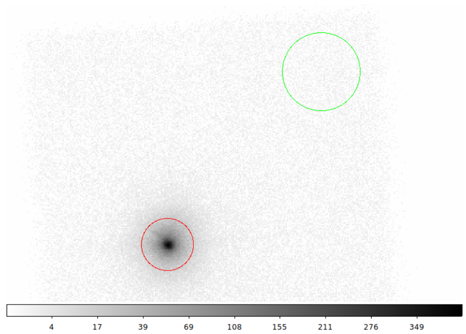

(a) FPMA

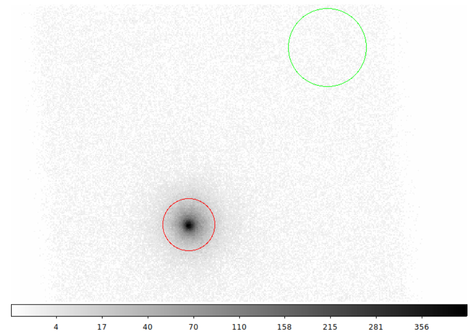

(b) FPMB

Figure 3.10: Images obtained from the observation taken on June 2018

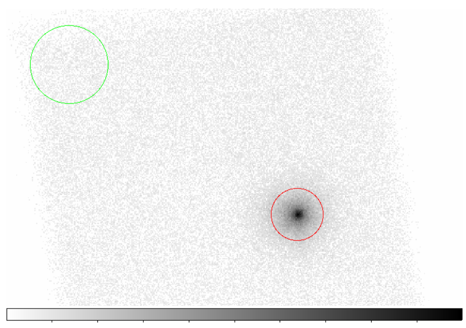

(a) FPMA

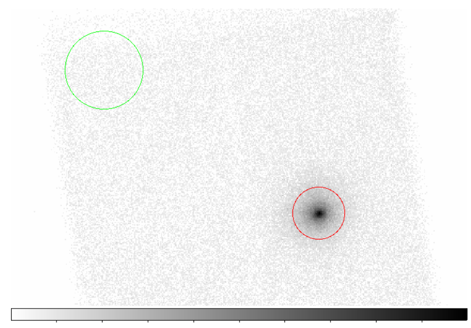

(b) FPMB

Figure 3.11: Images obtained from the observation taken on October 2018

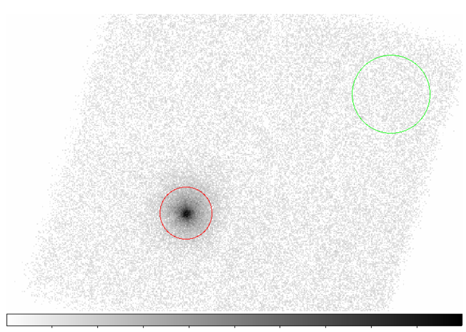

(a) FPMA

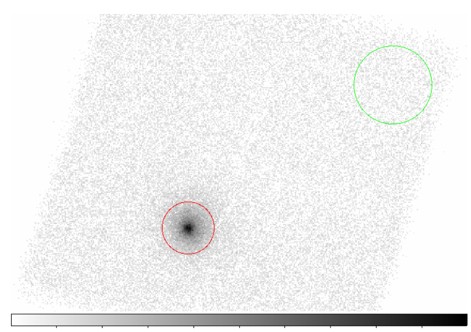

(b) FPMB

Figure 3.12: Images obtained from the observation taken on June 2019

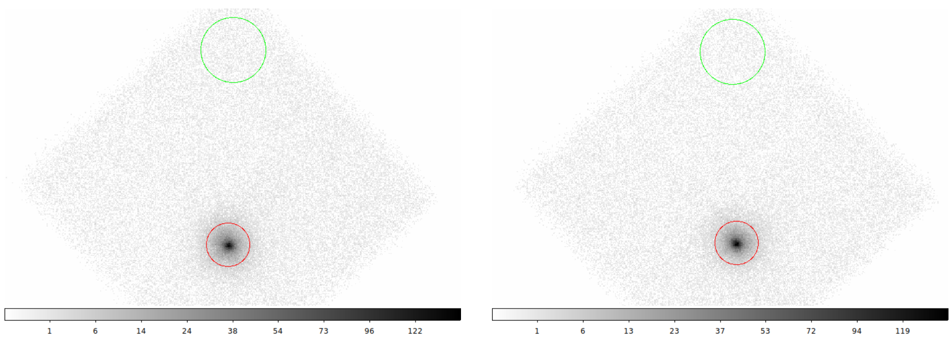

(a) FPMA (b) FPMB

Figure 3.13: Images obtained from the observation taken on August 2019

Chapter 4

Results of X-ray spectral fitting

4.1 Cross normalisation constants

Since we are analysing data from two space crafts and their different detectors, we need to explore systematic changes in cross-normalisation. We require the same parameters of a fit for all data sets belonging to one observation date. We freeze the pn constant to 1 and leave other constants as free parameters. We repeat it four times and then we make an average of obtained values. We do not include data from the last observation because XMM and NuSTAR observation start time is shifted by $\sim$3 days and it could have a strong impact to our cross normalisation values. Obtained constants are consistent within the range defined by Madsen et al. (2017). We do not use values listed in Madsen et al. (2017) because cross normalisation constants between XMM detectors are in energy interval 1–5 keV and between NuSTAR and XMM detectors from 3 to 7 keV, however we need to determine constants in the interval 3–10 keV. At last, cross normalisation constant depends also on spectrum of the source of specific observation. Our final values are given in Table 4.1.

Table 4.1: Cross normalisation constants.

	pn	MOS1	MOS2	FPMA	FPMB
pn	1	1.08 ± 0.01	1.08 ± 0.03	1.03 ± 0.02	1.07 ± 0.02

4.2 Spectral models

Power-law

A pure power-law spectrum with a constant spectral index is the signature of synchrotron radiation. The power-law continuum is believed to originate through the Compton up-scattering of the thermal photons by the electrons in a hot corona. The form of the power-law is

$$A\,(E) = KE^{-\Gamma}, \tag{4.1}$$

where K is a normalisation in photons/keV/cm^2 at 1 keV and Γ is a photon index of the power-law.

Zgauss

This model is a Gaussian function that takes redshift into account. The form of redshifted Gaussian is

$$A\,(E) = K \frac{1}{(1+z)\,\sigma\sqrt{2\pi}} \exp\left\{ \frac{-\left(E\,(1+z) - E_l\right)^2}{2\sigma^2} \right\}, \tag{4.2}$$

where E_l is a source frame line energy in keV, σ is a source frame line width in keV, z is a redshift and K is a source frame total photons/cm^2/s in the line.

4.3 Spectral analysis

We fit the data in *XSPEC* version 12.11.1. We try to re-analyse the data the same way as in Parker et al. (2019) but we have concluded that in some points we have different opinions. For these reason, we do the further analysis.

Firstly we load only the pn data and restrict them to the energy interval from 0.5 to 10 keV. As we fit them with a *power-law*, we can observe that this model gives us a good fit except for the observation taken in June 2018, where the spectrum shape changes. Then we added other spectra belonging to the specific observation date which means spectra from MOS1, MOS2, FPMA and FPMB detectors. We focus only on hard spectra in the energy range from 3 to 10 keV for the XMM-Newton spectra and from 3 to 75 keV for NuSTAR, because to fit data from this energy range, the simple model with two free parameters is adequate, so there is lower probability to stay in local minimum. Another reason is that for flux comparison we will use only overlapped energy interval from 3 to 10 keV (as we mentioned in section 3.1, XMM-Newton detectors are sensitive in a range from 0.2 to 10 keV and

(a) Goodness of the spectral fit.

Date	χ^2/dof
November 2015	180/209
June 2018	1586/1450
October 2018	1266/1096
June 2019	913/857
August 2019	777/764

(b) Flux in an energy range 3–10 keV.

Date	Flux [erg/cm^2/s]$\times 10^{-11}$
November 2015	0.22 ± 0.01
June 2018	5.36 ± 0.27
October 2018	1.38 ± 0.05
June 2019	0.92 ± 0.03
August 2019	1.56 ± 0.06

NuSTAR detectors from 3 to 75 keV). The exposure start time is not exactly the same for these two observatories, and there are also some calibration differences between detectors; we need to explore for cross normalisation constant as we describe in section 4.1. We fit spectra with *power-law* multiplied by *constant* where the obtained cross normalisation constant's values are fixed. We add a redshifted Gaussian line at 6.4 keV where we freeze just redshift to the value 0.005.

Therefore we freeze all obtained parameter values and we add also other models for example absorption model *tbabs*, distant reflection model *xillver* or relativistic reflection model *relxill* as was done in Parker et al. (2019). It does not improve the fit, likely because we analyse spectra above 3 keV, so it is unnecessary for this part of spectra and model *constant*∗(*powerlaw*+*zgauss*) is sufficient and it gives us a good overall fit. Reduced Chi-square for every observation date is listed in Table 4.2a.

We plot data and the result folded models with *Python*. Individual plots for each observation date are shown in Figures 4.1, 4.2, 4.3, 4.4 and 4.5. Best fit parameters for all observations are listed in Table 4.3, where the "norm." is a normalisation with subscript denoting different detectors.

To determine flux we discuss two methods. The first one is to add *cflux* as a model component with three parameters E_{min}, E_{max} and *lg10flux*. Parameters E_{min} and E_{max} delimit an interval to determine the flux. Parameter *lg10flux* is the decimal logarithm of the flux. We fixed E_{min} to the value of 3 and E_{max} to the value of 10 keV. We left parameter *lg10flux* free for all spectra. This method does not give us satisfying values because they are many orders far away from each other and they are not physically interpretable.

The second method is the *flux* command which has been a better way of determining flux. It calculates the flux for the specified energy range for every spectrum separately. As our spectra overlap in an interval of 3 to 10 keV, we determined flux from this range. As the resulting flux value, we choose the average value from all spectra belonging to the one observation date.

Results of the flux determination are: Flux of NGC 1566 increased by a factor of 25 between November 2015 and June 2018 (see Table 4.2b). Last XMM-Newton observation is affected by flaring background so we consider only NuSTAR data for this date. The second most strong outburst occurred in August 2019. Compared to previous observation taken on June 2019 it increased by a factor of 2 in just two months.

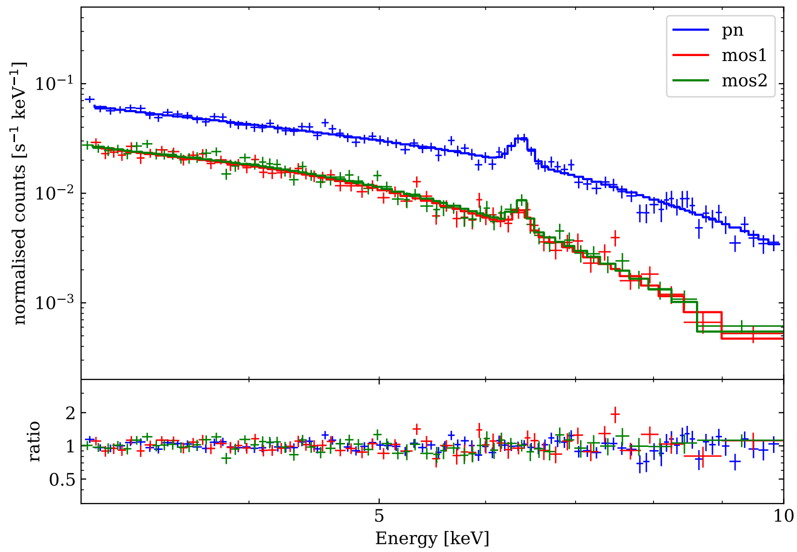

Figure 4.1: Best-fit broad-band XMM-Newton spectra from November 2015.

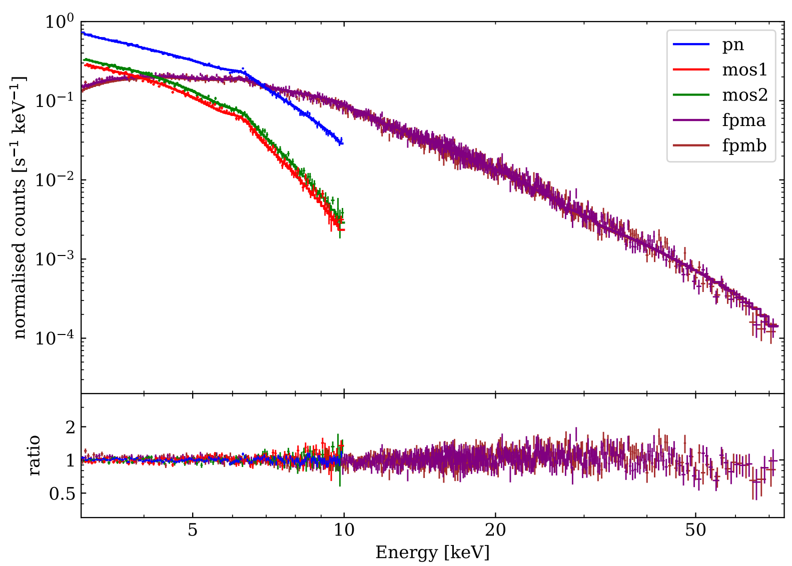

Figure 4.2: Best-fit broad-band XMM-Newton and NuSTAR spectra from June 2018.

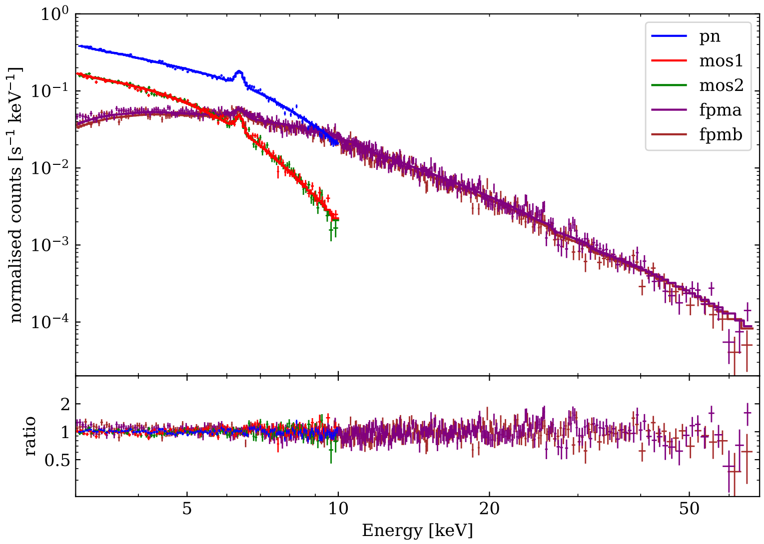

Figure 4.3: Best-fit broad-band XMM-Newton and NuSTAR spectra from October 2018.

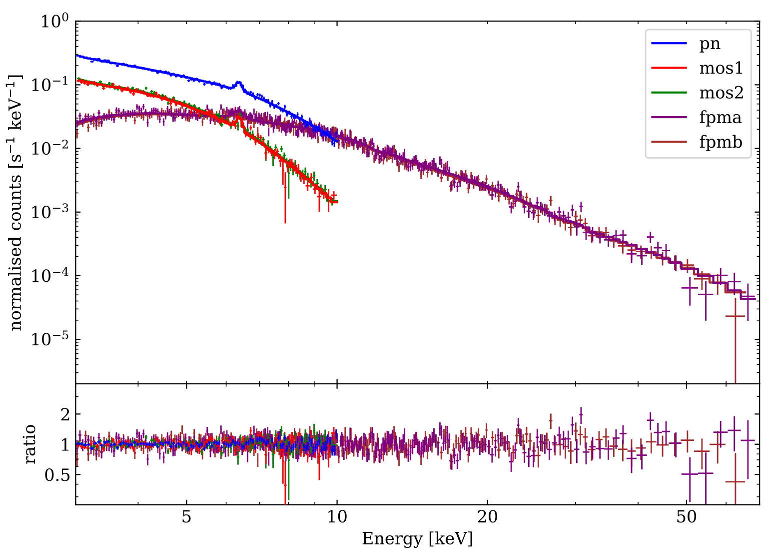

Figure 4.4: Best-fit broad-band XMM-Newton and NuSTAR spectra from June 2019.

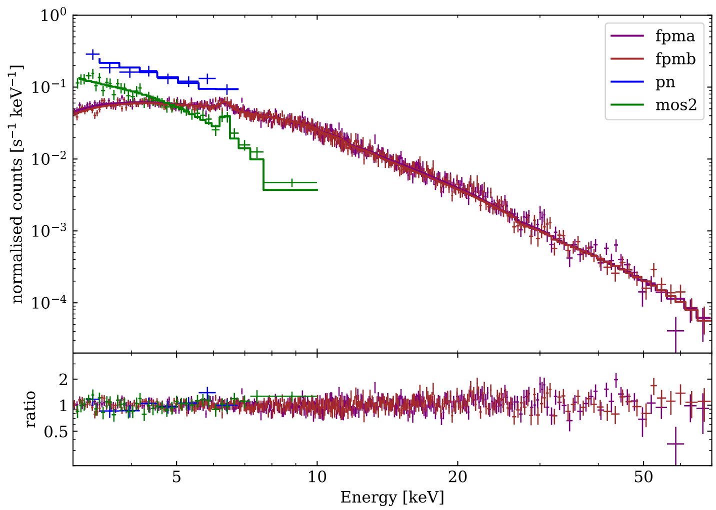

Figure 4.5: Best-fit broad-band XMM-Newton and NuSTAR spectra from August 2019.

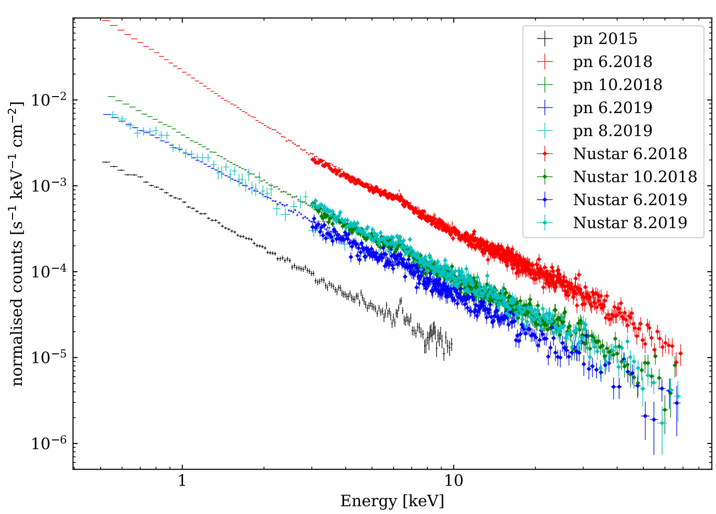

Figure 4.6: XMM-Newton and NuSTAR spectra. The data are corrected for the effective area of the instruments. For clarity, we show only the EPIC-pn and FPMA NuSTAR data.

Table 4.3: Best fit parameters. Both $E_{\rm line}$, $\sigma_{\rm line}$ in keV.

Parameter	11/2015	6/2018	10/2018	6/2019	8/2019
power-law					
Γ	1.55 ± 0.01	1.65 ± 0.01	1.58 ± 0.01	1.62 ± 0.01	1.67 ± 0.01
norm.$_{\rm pn}$	$(4.72 \pm 0.09) \times 10^{-4}$	$(1.41 \pm 0.016) \times 10^{-2}$	$(3.22 \pm 0.05) \times 10^{-3}$	$(2.34 \pm 0.05) \times 10^{-3}$	$(2.42 \pm 0.26) \times 10^{-3}$
norm.$_{\rm mos1}$	$(4.73 \pm 0.13) \times 10^{-4}$	$(1.43 \pm 0.018) \times 10^{-2}$	$(3.21 \pm 0.06) \times 10^{-3}$	$2.32^{+0.06}_{-0.05} \times 10^{-3}$	–
norm.$_{\rm mos2}$	$(1.74 \pm 0.12) \times 10^{-4}$	$(1.45 \pm 0.018) \times 10^{-2}$	$(3.13 \pm 0.06) \times 10^{-3}$	$(2.30 \pm 0.05) \times 10^{-3}$	$(2.68 \pm 0.13) \times 10^{-3}$
norm.$_{\rm fpma}$	–	$(1.39 \pm 0.02) \times 10^{-2}$	$(3.34 \pm 0.08) \times 10^{-3}$	$2.35^{+0.08}_{-0.07} \times 10^{-3}$	$(4.23 \pm 0.13) \times 10^{-3}$
norm.$_{\rm fpmb}$	–	$(1.39 \pm 0.02) \times 10^{-2}$	$(3.28 \pm 0.08) \times 10^{-3}$	$2.40^{+0.08}_{-0.07} \times 10^{-5}$	$(4.30 \pm 0.13) \times 10^{-3}$
zgauss					
$E_{\rm line}$	6.40 ± 0.02	$6.27^{+0.04}_{-0.05}$	6.39 ± 0.01	$6.40^{+0.02}_{-0.01}$	6.40 ± 0.04
$\sigma_{\rm line}$	$2.79^{+63.5}_{-2.79} \times 10^{-3}$	(0.38 ± 0.05)	$7.75^{+1.92}_{-1.82} \times 10^{-2}$	$(3.22 \pm 3.22) \times 10^{-5}$	$1.19^{+0.77}_{-0.83} \times 10^{-1}$
norm.$_{\rm pn}$	$(4.78 \pm 1.07) \times 10^{-6}$	$8.40^{+1.34}_{-1.28} \times 10^{-5}$	$2.50^{+0.27}_{-0.26} \times 10^{-5}$	$9.68^{+1.76}_{-1.77} \times 10^{-6}$	$1.90^{+2.79}_{-1.90} \times 10^{-5}$
norm.$_{\rm mos1}$	$(2.83 \pm 1.53) \times 10^{-6}$	$1.59^{+0.28}_{-0.26} \times 10^{-4}$	$2.82^{+0.46}_{-0.44} \times 10^{-5}$	$(1.40 \pm 0.33) \times 10^{-5}$	–
norm.$_{\rm mos2}$	$(3.98 \pm 1.61) \times 10^{-6}$	$1.23^{+0.24}_{-0.23} \times 10^{-4}$	$2.46^{+0.47}_{-0.45} \times 10^{-5}$	$(1.07 \pm 0.33) \times 10^{-5}$	$3.70^{+1.89}_{-1.77} \times 10^{-5}$
norm.$_{\rm fpma}$	–	$8.43^{+1.62}_{-1.56} \times 10^{-5}$	$2.24^{+0.52}_{-0.51} \times 10^{-5}$	$1.69^{+0.45}_{-0.46} \times 10^{-5}$	$2.34^{+0.71}_{-0.66} \times 10^{-5}$
norm.$_{\rm fpmb}$	–	$7.72^{+1.57}_{-1.53} \times 10^{-5}$	$(2.53 \pm 0.52) \times 10^{-5}$	$(1.24 \pm 0.45) \times 10^{-5}$	$2.74^{+0.72}_{-0.67} \times 10^{-5}$

Chapter 5

Discussion

The X-ray spectrum of NGC 1566 is a standard spectrum for a Sy1 galaxy, showing a typical power-law slope of $\Gamma \sim 1.5 - 1.7$, and only little absorption ($n_{\rm H} = 9 \times 10^{19} {\rm cm}^{-2}$). We investigate the source in X-ray domain, and we confirm the dramatic flux change over five year period (chapter 4.3). On the other side, the source does not change observational properties from Compton thick to Compton thin, so we conclude that it is an optical changing look AGN. In this section we discuss possible interpretations of the NGC 1566 variability.

The variation obscuration theory (chapter 1.3.2) could be rejected in this case, because the spectral shape shows marginal changes. According to Oknyanskij et al. (2018), optical and UV changes were also discovered. It is not well physically interpretable to change in UV/optical bands in such a short time scales.

Another theory, considered in Parker et al. (2019), is an instability in the accretion disc. In that case, the inner disc is in a low state until radiation pressure exceeds gas pressure. If this occurs, an accretion disc can switch on to a higher state. This mechanism was also considered in Śniegowska et al. (2020), where they concentrate on modelling the repeating semi-regular outburst. According to their model, the radiation pressure instability between the outer gas-dominated stable disc, and an inner hot advection-dominated accretion flow, may explain the outburst behaviour of NGC 1566, but it cannot explain results presented in Oknyanskij et al. (2018) because the rise time is not longer than the decay time.

Next eligible theory is the tidal disruption event scenario. Oknyanskij et al. (2018) considered it as a plausible explanation. In that paper, they explain that tidal stripping of a star could cause frequent and recurrent events, and also, these events could initiate accretion disc instabilities and explain short time scales for brightening, as well as their repeating. Chan et al. (2019) modelled tidal disruption events in AGNs.

They present that these TDEs could be confused with common AGN flares. Their simulations consistently show that the collision of the bound debris of a TDE with pre-existing accretion disc could induce shocks in the disc. They explain that, as a result, the disc interior to the stream impact point is heated to high temperatures and evacuated on timescales much shorter than the mass return time. This theory is dismissed in Parker et al. (2019).

The last discussed interpretation is change of an accretion state (chapter 1.3.2). Spectral changes are similar to those of XRBs but if we consider these theory it signify that standard thin disc can evolve much faster than expected from a simple extrapolation of typical accretion disc time scales observed in XRBs.

Chapter 6

Conclusion

NGC 1566 has shown interesting behaviour which opens many questions about our current understanding of active galactic nuclei and processes operating there. In this thesis we summarize commonly accepted brief AGN.

The studied period covers the latest outburst: from 2015 to 2019 with a peak in 2018. We reduced XMM and Nustar data of NGC 1566 and performed spectral fitting in 3-75 keV energy domain

We compared (chapter 4.3, Table 4.2b) the obtained flux from five different observations. Our results are consistent with data obtained from other instruments at other wavelengths presented in referenced publications (Oknyanskij et al. (2018), Śniegowska et al. (2020), Parker et al. (2019)), and they show a strong outburst in 2018, and also another outburst in August 2019.

We discuss possible mechanisms for unusual behaviour. NGC 1566 is not only a good candidate for understanding the changing-look phenomenon but this very variable phenomenon could be also an important part of AGN knowledge. A multi-wavelength long-term observations of such sources are necessary to clarifications of many remaining questions about AGNs. NGC 1566 one of the key source that could help to shed light on this phenomenon.

Bibliography

Antonucci, R. R. J. and Miller, J. S. (1985). Spectropolarimetry and the nature of NGC 1068. *ApJ*, 297:621–632.

Beckmann, V. and Shrader, C. R. (2013). The agn phenomenon: open issues.

Boller, T., Brandt, W. N., Fabian, A. C., and Fink, H. H. (1997). ROSAT monitoring of persistent giant and rapid variability in the narrow-line Seyfert 1 galaxy IRAS 13224-3809. *Monthly Notices of the Royal Astronomical Society*, 289(2):393–405.

Carroll, B. W. and Ostlie, D. A. (2007). *An introduction to modern astrophysics; 2nd ed.* Addison-Wesley, San Francisco, CA.

Chan, C.-H., Piran, T., Krolik, J. H., and Saban, D. (2019). Tidal disruption events in active galactic nuclei. *The Astrophysical Journal*, 881(2):113.

Denney, K. D., Rosa, G. D., Croxall, K., Gupta, A., Bentz, M. C., Fausnaugh, M. M., Grier, C. J., Martini, P., Mathur, S., Peterson, B. M., Pogge, R. W., and Shappee, B. J. (2014). THE TYPECASTING OF ACTIVE GALACTIC NUCLEI: Mrk 590 NO LONGER FITS THE ROLE. *The Astrophysical Journal*, 796(2):134.

ESA (2021a). `https://directory.eoportal.org/web/eoportal/satellite-missions/content/-/article/xmm-newt-1`. [Online; accessed 08-June-2021].

ESA (2021b). `http://nxsa.esac.esa.int/nxsa-web/#search`. [Online; accessed 08-June-2021].

ESA (2021c). `https://www.cosmos.esa.int/web/xmm-newton/sas-threads`. [Online; accessed 08-June-2021].

Fender, R. P., Belloni, T. M., and Gallo, E. (2004). Towards a unified model for black hole X-ray binary jets. *MNRAS*, 355(4):1105–1118.

Gaskell, M. and Klimek, E. (2003). Variability of active galactic nuclei from the optical to x-ray regions. *Astronomical and Astrophysical Transactions*, 22(4-5):661–679.

Guainazzi, M. (2002). The formerly X-ray reflection-dominated Seyfert 2 galaxy NGC 6300. *Monthly Notices of the Royal Astronomical Society*, 329(1):L13–L17.

Habibi, A. and Abbassi, S. (2019). Thermal instability of thin accretion disks in the presence of wind and a toroidal magnetic field. *The Astrophysical Journal*, 887(2):256.

Khachikian, E. Y. and Weedman, D. W. (1974). An atlas of Seyfert galaxies. *ApJ*, 192:581–589.

Kollatschny, W., Grupe, D., Parker, M., Ochmann, M., Schartel, N., Herwig, E., Komossa, S., Romero-Colmonero, E., and Santos-Lleo, M. (2020). Optical and x-ray discovery of the changing-look agn iras 23226-3843 showing extremely broad and double-peaked balmer profiles. *Astronomy & Astrophysics*, 638.

Körding, E., Falcke, H., and Corbel, S. (2006). Refining the fundamental plane of accreting black holes. *Astronomy & Astrophysics*, 456(2):439–450.

MacLeod, C. L., Green, P. J., Anderson, S. F., Bruce, A., Eracleous, M., Graham, M., Homan, D., Lawrence, A., LeBleu, A., Ross, N. P., Ruan, J. J., Runnoe, J., Stern, D., Burgett, W., Chambers, K. C., Kaiser, N., Magnier, E., and Metcalfe, N. (2019). Changing-look quasar candidates: First results from follow-up spectroscopy of highly optically variable quasars. *The Astrophysical Journal*, 874(1):8.

MacLeod, C. L., Ross, N. P., Lawrence, A., Goad, M., Horne, K., Burgett, W., Chambers, K. C., Flewelling, H., Hodapp, K., Kaiser, N., and et al. (2016). A systematic search for changing-look quasars in sdss. *Monthly Notices of the Royal Astronomical Society*, 457(1):389–404.

Madsen, K. K., Beardmore, A. P., Forster, K., Guainazzi, M., Marshall, H. L., Miller, E. D., Page, K. L., and Stuhlinger, M. (2017). IACHEC Cross-calibration of Chandra, NuSTAR, Swift, Suzaku, XMM-Newton with 3C 273 and PKS 2155-304. *AJ*, 153(1):2.

Matt, G., Guainazzi, M., and Maiolino, R. (2003). Changing look: from Compton-thick to Compton-thin, or the rebirth of fossil active galactic nuclei. *Monthly Notices of the Royal Astronomical Society*, 342(2):422–426.

Matt, G., Perola, G. C., and Piro, L. (1991). The iron line and high energy bump as X-ray signatures of cold matter in Seyfert 1 galaxies. *A&A*, 247:25.

Middei, R., Vagnetti, F., Bianchi, S., La Franca, F., Paolillo, M., and Ursini, F. (2017). A long-term study of agn x-ray variability - structure function analysis on a rosat-xmm quasar sample. *Astronomy & Astrophysics*, 599:A82.

Mineshige, S. (1993). Accretion Disk Instabilities. *Ap&SS*, 210(1-2):83–103.

NASA (2020a). https://heasarc.gsfc.nasa.gov/docs/xmm/xmm.html. [Online; accessed 08-June-2021].

NASA (2020b). https://heasarc.gsfc.nasa.gov/docs/nustar/analysis/nustar_swguide.pdf. [Online; accessed 08-June-2021].

NASA (2021). https://heasarc.gsfc.nasa.gov/db-perl/W3Browse/w3table.pl?tablehead=name%3Dnumaster&Action=More+Options. [Online; accessed 08-June-2021].

Nemiroff, R. and Bonnell, J. (2019). https://apod.nasa.gov/apod/ap190702.html. [Online; accessed 10-June-2021].

Ochmann, M., Kollatschny, W., and Zetzl, M. (2020). Spectral changes and BLR kinematics of eruptive changing-look AGN. *Contributions of the Astronomical Observatory Skalnaté Pleso*, 50(1):318–327.

Oknyanskij, V., Winkler, H., Tsygankov, S., Lipunov, V., Gorbovskoy, E., Wyk, F., Buckley, D., and Tyurina, N. (2018). New changing look case in ngc 1566.

Osterbrock, D. E. and Koski, A. T. (1976). NGC 4151 and Markarian 6 - two intermediate-type Seyfert galaxies. *MNRAS*, 176:61P–66P.

Parker, M. L., Schartel, N., Grupe, D., Komossa, S., Harrison, F., Kollatschny, W., Mikula, R., Santos-Lleó, M., and Tomás, L. (2019). X-ray spectra reveal the reawakening of the repeat changing-look AGN NGC 1566. M.N.R.A.S., 483(1):L88–L92.

Pastoriza, M. and Gerola, H. (1970). Spectral Variation in the Seyfert Galaxy NGC 1566. *Astrophys. Lett.*, 6:155.

Quintana, H., Kaufmann, P., and Sérsic, J. L. (1975). Activity of the Nucleus of the Southern Seyfert Galaxy NGC 1566. *Monthly Notices of the Royal Astronomical Society*, 173(1):57P–60P.

Reeves, J. N., Wynn, G., O'Brien, P. T., and Pounds, K. A. (2002). Extreme x-ray variability in the luminous quasar pds 456. *Monthly Notices of the Royal Astronomical Society*, 336(3):L56–L60.

Risaliti, G., Elvis, M., Fabbiano, G., Baldi, A., and Zezas, A. (2005). Rapid compton-thick/compton-thin transitions in the seyfert 2 galaxy NGC 1365. *The Astrophysical Journal*, 623(2):L93–L96.

Rossi, E., Stone, N., Law-Smith, J., MacLeod, M., Lodato, G., Dai, L., and Mandel, I. (2020). The process of stellar tidal disruption by supermassive black holes. the first pericenter passage.

Saxton, C., Perets, H., and Baskin, A. (2018). Spectral features of tidal-disruption candidates and alternative origins for such transient flares. *Monthly Notices of the Royal Astronomical Society*, 474:3307–3323.

Sobolewska, M. A., Siemiginowska, A., and Gierliński, M. (2011). Simulated spectral states of active galactic nuclei and observational predictions. *Monthly Notices of the Royal Astronomical Society*, 413(3):2259–2268.

Svoboda, J., Guainazzi, M., and Merloni, A. (2017). Agn spectral states from simultaneous uv and x-ray observations by xmm-newton. *Astronomy & Astrophysics*, 603:A127.

Zhao (unknown). https://science.clemson.edu/ctagn/project/. [Online; accessed 07-June-2020].

Śniegowska, M., Czerny, B., Bon, E., and Bon, N. (2020). Possible mechanism for multiple changing-look phenomena in active galactic nuclei. *Astronomy & Astrophysics*, 641.

Created in LaTeX